Available online at www.sciencedirect.com
ScienceDirect
Polymer 48 (2007) 6867–6880
polymer
www.elsevier.com/locate/polymer

The role of interlamellar chain entanglement in deformation-induced structure changes during uniaxial stretching of isotactic polypropylene

Feng Zuo [a], Jong Kahk Keum [a], Xuming Chen [a], Benjamin S. Hsiao [a,*], Hongyu Chen [b], Shih-Yaw Lai [b], Ronald Wevers [b], Jing Li [c]

[a] *Department of Chemistry, Stony Brook University, Stony Brook, NY 11794-3400, United States*
[b] *Performance Plastics and Chemicals, The Dow Chemical Company, Freeport, TX 77541, United States*
[c] *Core Research and Development, Materials Science, The Dow Chemical Company, Freeport, TX 77541, United States*

Received 29 June 2007; received in revised form 29 August 2007; accepted 30 August 2007
Available online 14 September 2007

Abstract

In-situ small-angle X-ray scattering (SAXS), and wide-angle X-ray diffraction (WAXD) were carried out to investigate the deformation-induced structure changes of isotactic polypropylene (iPP) films during uniaxial stretching at varying temperatures (room temperature, 60 °C and 160 °C). From the WAXD data, mass fractions of amorphous, mesomorphic and crystal phases were estimated. Results indicate that at room temperature, the dominant structure change is the transformation of folded-chain crystal lamellae (monoclinic α-form) to oriented mesomorphic phase; while at high temperatures (>60 °C); the dominant change is the transformation of amorphous phase to oriented folded-chain crystal lamellae. This behavior may be explained by the relative strength between the interlamellar entangled network of amorphous chains, which probably directly influence the tie chain distribution, and the surrounding crystal lamellae. It appears that during stretching at low temperatures, the interlamellar entanglement network is strong and can cause lamellar fragmentation, resulting in the formation of oriented mesomorphic phase. In contrast, during stretching at high temperatures, the chain disentanglement process dominates, resulting in the relaxation of restrained tie chains and the formation of more folded-chain lamellae.

Keywords: Polypropylene; Deformation; Entanglement

1. Introduction

It is well understood that molten polymer chains are entangled in a dynamic manner, where the variation of temperature does not alter the average length between the entanglement points (i.e., the entanglement length) or the entanglement density [1,2]. However, during crystallization, chains can be disentangled and the residual entanglements will be pushed into the interlamellar amorphous region. With the decrease in temperature, the event of crystallization can result in the retention or even an increase of the entanglement density in the interlamellar amorphous domain of semi-crystalline polymers [3].

In the past, mechanical properties of semi-crystalline polymers have often been related to crystallinity, crystalline structure and morphology [4–9], amorphous chain orientation, as well as distribution and concentration of tie chains in the interlamellar amorphous region [10–18]. In these variables, the concept of tie chains is the most illusive one, since they cannot be easily measured experimentally or predicted theoretically. In this study, we hypothesize that the entanglement network of amorphous chains in the interlamellar region directly influences the formation of tie chains, thus playing a vital role to affect the overall mechanical behavior and deformation-induced structure/morphology changes. Of course, some tie chains are not resulted from the chain entanglements, but we

* Corresponding author. Tel.: +1 631 632 7793; fax: +1 631 632 6518.
E-mail address: bhsiao@notes.cc.sunysb.edu (B.S. Hsiao).

0032-3861/$ - see front matter © 2007 Elsevier Ltd. All rights reserved.
doi:10.1016/j.polymer.2007.08.065

speculate that the amount of such species may be small. The advantage of the entanglement-induced tie chains concept is that it may allow us to relate the solid state topology of entangled chains in the interlamellar region with molecular theories of rheology. Although the experimental design in the present study did not allow us to directly test the effect of interlamellar chain entanglement on the mechanical properties (this will be carried out later using samples of bimodal blends with different molecular weights, where the entanglement density can be systematically change), the results indeed are consistent with the concept of entanglement-induced tie chains in the interlamellar region.

Isotactic polypropylene (iPP) was chosen as a model compound in this work for the following reasons. It is well known that iPP has hierarchical structures, including micro-scale spherulites, nano-scale crystalline lamellae and atomic-scale crystal unit cells, typical of semi-crystalline polymers. The relationship between mechanical deformation and structure change at different length scales in iPP has been well documented. For example, Keller et al. studied the deformation behavior of micro-scale spherulites. They observed both homogenous and inhomogeneous deformation pathways within and between the spherulites [19]. Shimamura investigated the temperature dependence of spherulite change during deformation. They reported that deformation began in the equatorial region of spherulite at low temperatures, but in the meridional region at high temperatures [20]. The finding suggested that the applied stress was quite localized in the spherulite, which might reflect the variation of chain topology in the lamellar morphology. The stress localization can occur when some chain defects are pushed out from the crystalline region during crystallization. These defects will include the dangling chain ends that cannot carry stress, but they will not include stereo defects and self-looping that can carry stress. The stress localization can also occur when some amorphous chains (e.g. tie chains) carry more stress than the rest of the chains.

In iPP, the deformation-induced morphology and structure changes have been well documented. On a large scale, Peterlin [21,22] reported that spherulites could be transformed into oriented fibrils above the yield point, passing through the stages of elastic deformation, plastic deformation, fragmentation of the lamellar structure, formation of fibrillar structure at high strains. From the conventional viewpoint, the deformation mechanism in semi-crystalline polymers usually includes interlamellar and intralamellar slipping of the superstructure, chain pulling-out from the folded-chain lamellae (sometimes termed mechanically-induced melting), and recrystallization and formation of oriented extended-chain crystals [23–31]. Strobl et al. [32] argued that tensile deformation of semi-crystalline polymers could be considered as stretching of interpenetrated network of crystalline domains (blocks). In their model, the crystalline block can slip at small strains; but it will disintegrate and recrystallize above a critical stress. During deformation of some polymers, polymorphic transformations are also known to take place. The metastable crystal structure can prevail under strained conditions because of the reduced entropy. This behavior has been seen in iPP [33,34] as well as in poly(ethylene terephthalate) [35–38].

The mesomorphic form of iPP was first discovered by Natta et al. [39,40] through quenching of the melt into ice water. Later it was found that the mesomorphic phase could also be obtained by cold drawing of iPP films at room temperature [41,42]. The mesomorphic form can be identified by the appearance of two broad peaks in the wide-angle X-ray powder diffraction pattern (or a 6-point feature in the fiber diffraction pattern), located at 2θ angles of 14.8° and 21.2° (based on Cu Kα radiation), respectively. The location of the 14.8° peak is close to that of the diffuse amorphous peak from the iPP melt, but the presence of the 21.2° peak indicates a higher order of structure from the helical chains. The infrared spectra indicates that the mesomorphic phase contains the 3_1 helical chain conformation that is very similar to that in the monoclinic crystal structure [43–46]. The mesomorphic phase in iPP can transform into the monoclinic α-form when annealed at temperatures above 60 °C [47–50], although there seems to be a saturation level associated with the annealing time, which is a function of temperature.

Recently, there have been several in-situ and ex-situ deformation studies on polyolefin (including iPP and polyethylene, PE) using synchrotron X-ray, atomic forced microscopy (AFM), birefringence, optical microscopy (OM), electron microscopy (EM) and infrared spectroscopy (IR) techniques [51–63]. These studies revealed the different effects of molecular variables including tacticity, crystal forms, catalyst used, MWD (molecular weight distribution) on the deformation behavior of olefin-based semi-crystalline polymers. In the present study, we carried out an in-situ deformation study of iPP using combined synchrotron X-ray scattering and diffraction methods. The general results were found to be consistent with the model proposed by Peterlin [21,22]. However, the difference between low and high temperature results implied the distinct role of interlamellar chain entanglement in deformation-induced structure changes. In iPP, the unique transformation from folded-chain α-form crystals to extended-chain mesomorphic phase (detectable by wide-angle X-ray diffraction, WAXD) was the key that permitted us to make such an observation, whereas the lack of unique structure change in PE would make the similar X-ray investigation very difficult.

Based on the experimental results, we hypothesize that the existence of chain entanglements in the interlamellar amorphous region dictates the distribution of tie chains; where the strength of the entanglement network can directly affect the stability of adjacent crystal lamellae. Two likely scenarios can be used to rationalize this hypothesis. (1) The interlamellar amorphous region contains entangled chains, whose entanglement density may be even higher than that in the initial amorphous bulk. (2) Temperature does not change the interlamellar entanglement density, but significantly alters the chain mobility. At low temperatures, the entanglement can be considered frozen because the chain dynamics is very slow; at high temperatures, the disentanglement may occur during stretching through slippage. It is conceivable that the

above behavior may be universal in all semi-crystalline polymers.

2. Experimental

2.1. Materials and preparation

In this study, a conventional Ziegler–Natta isotactic polypropylene (iPP) homopolymer was used. The material had a melt flow index of 3.2 (at 230 °C, 2.16 kg) and a DSC melting point of about 165 °C. This commercial material had an average molecular weight (M_w) of about 300 kg/mol and was used in the form of partially oriented film. The films were produced from a 20 mm 25 D extruder, equipped with a horizontal flat die and a three roll calendar stack. The extrusion was carried out at 240 °C and 10 mm/s, where the film was cast onto a chill roll with direct contact from the top roll.

2.2. Characterization methods

In-situ wide-angle X-ray diffraction (WAXD) and small-angle X-ray scattering (SAXS) studies were carried out at the X27C beam line in the National Synchrotron Light Source (NSLS), Brookhaven National Laboratory (BNL). The wavelength of the synchrotron radiation was 1.371 Å. A three-pinhole collimation system was used to reduce the beam size to 0.6 mm in diameter. Two-dimensional (2D) WAXD and SAXS patterns were collected by a MAR CCD X-ray detector (MAR-USA), which had a resolution of 1024 × 1024 pixels (pixel size = 158.44 μm). The typical image acquisition time was 20 s for each data frame. The sample-to-detector distance was around 1850 mm for SAXS (calibrated by a silver behenate (AgBe) standard), and was around 100 mm for WAXD (calibrated by an aluminum oxide (Al_2O_3) standard). All X-ray images were corrected for background scattering, air scattering and beam fluctuations.

Uniaxial tensile deformation was performed with a modified Instron 4442 tensile apparatus, which could stretch the film symmetrically. The symmetric stretching guaranteed that the focused X-ray beam could illuminate the same sample position during deformation. The original length of the sample between the Instron clamps was 14 mm. A constant deformation rate, 10 mm/min, was applied to the specimen throughout the deformation study. The deformation experiments were carried out at room temperature (about 25 °C), 60 °C and 160 °C, respectively. The stress and strain mentioned in this study are all engineering stress and engineering strain measured directly from the Instron machine. The heating chamber for this Instron apparatus was about 240 mm in length, which meant that the highest attainable engineering strain was only about 16.0.

2.3. X-ray data analysis

A semi-quantitative SAXS analysis was carried out to determine the changes of lamellar structure (e.g. long spacing) from the meridional scattering peaks, and the formation of fibrillar structure from the equatorial streak that might be tainted with the occurrence of micro-voids [64–66]. As the emphasis in this study was on the structure change, the WAXD results were analyzed quite extensively using the following procedures.

All 2D WAXD patterns were first corrected by the Fraser method to compensate the effect of flat-plate detection [67], and then for the background and air scattering. The corrected pattern was deconvoluted into two parts, isotropic and anisotropic contributions (see Fig. 1), using a ‘‘halo method’’ [68]. The isotropic contribution can be attributed to unoriented species, including amorphous and unoriented crystal phases; while the anisotropic contribution can be attributed to oriented species, including oriented mesomorphic and crystal phases. The principle for this deconvolution approach is that the

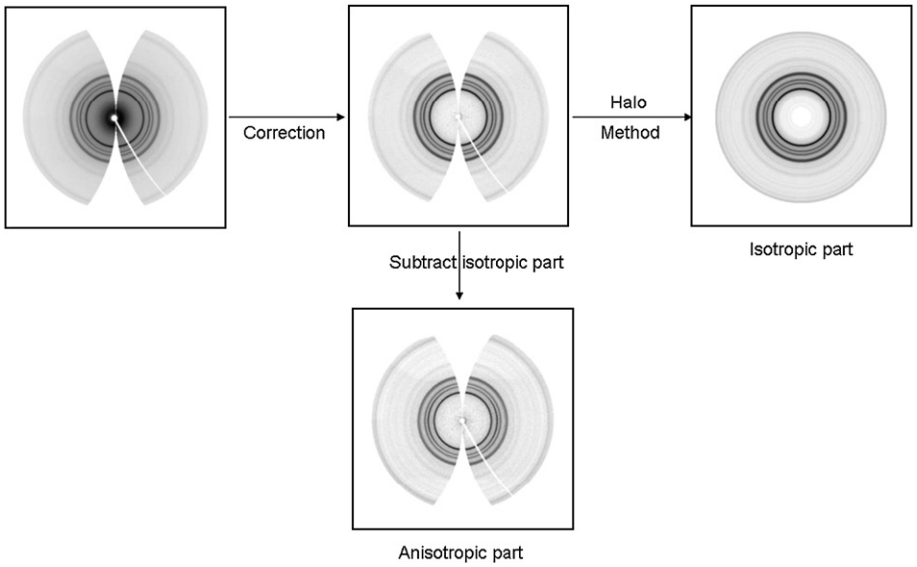

Fig. 1. Procedures for deconvolution of isotropic and anisotropic contributions from a Fraser-corrected 2D WAXD pattern.

azimuthally independent component in the total scattered profile is directly proportional to the unoriented fraction of the scatterer, which can be determined as follows. For each azimuthal scan at a specific scattering angle (2θ), the minimum value of the intensity profile can be considered as the envelope intensity of the unoriented species at that angle. By extracting all the minimum values at all scattering angles, a 2D image of the isotropic contribution is generated. This isotropic contribution is then subtracted from the total scattering image, yielding the oriented contribution. Assuming that stretched samples have a cylindrical rotational symmetry, which is true especially for samples at high strain (patterns, not shown here, taken from three orthogonal directions prove that the sample has cylindrical rotational symmetry), and a 2D pattern can contain the complete information to describe the intensity distribution in reciprocal space, and integrating over such 2D sections through 3D reciprocal space will produce the fractions of each phase. The anisotropic fraction is circularly averaged into a linear intensity profile, which can be deconvoluted into crystal and mesomorphic fractions by using the method of one-dimensional peak fitting. The same method is also applied to analyze the isotropic contribution, where the fractions of unoriented crystal and amorphous phases can be obtained. The total crystallinity index (termed crystallinity hereafter, as they are proportional to each other) is estimated by the sum of the fractions from oriented and unoriented crystal phases.

3. Results and discussion

3.1. Uniaxial tensile deformation at room temperature

The engineering stress–strain curve of iPP film during uniaxial tensile deformation at room temperature (about 25 °C), together with selected 2D WAXD and SAXS patterns collected at different applied strains, are shown in Fig. 2. It is seen that the orientation of the initial sample is very low. In the first 2D WAXD pattern, several nearly isotropic diffraction rings were detected, which could be indexed as (110), (040), (130) and (111)/(041), respectively (from inner to outer) using the α-form monoclinic iPP crystal structure. The corresponding SAXS pattern also exhibited a nearly isotropic ring, indicating the existence of a lamellar structure with a slight orientation. This observation is consistent with the initial spherulitic structure observed by AFM, which will be discussed later. The long period, that is the average distance

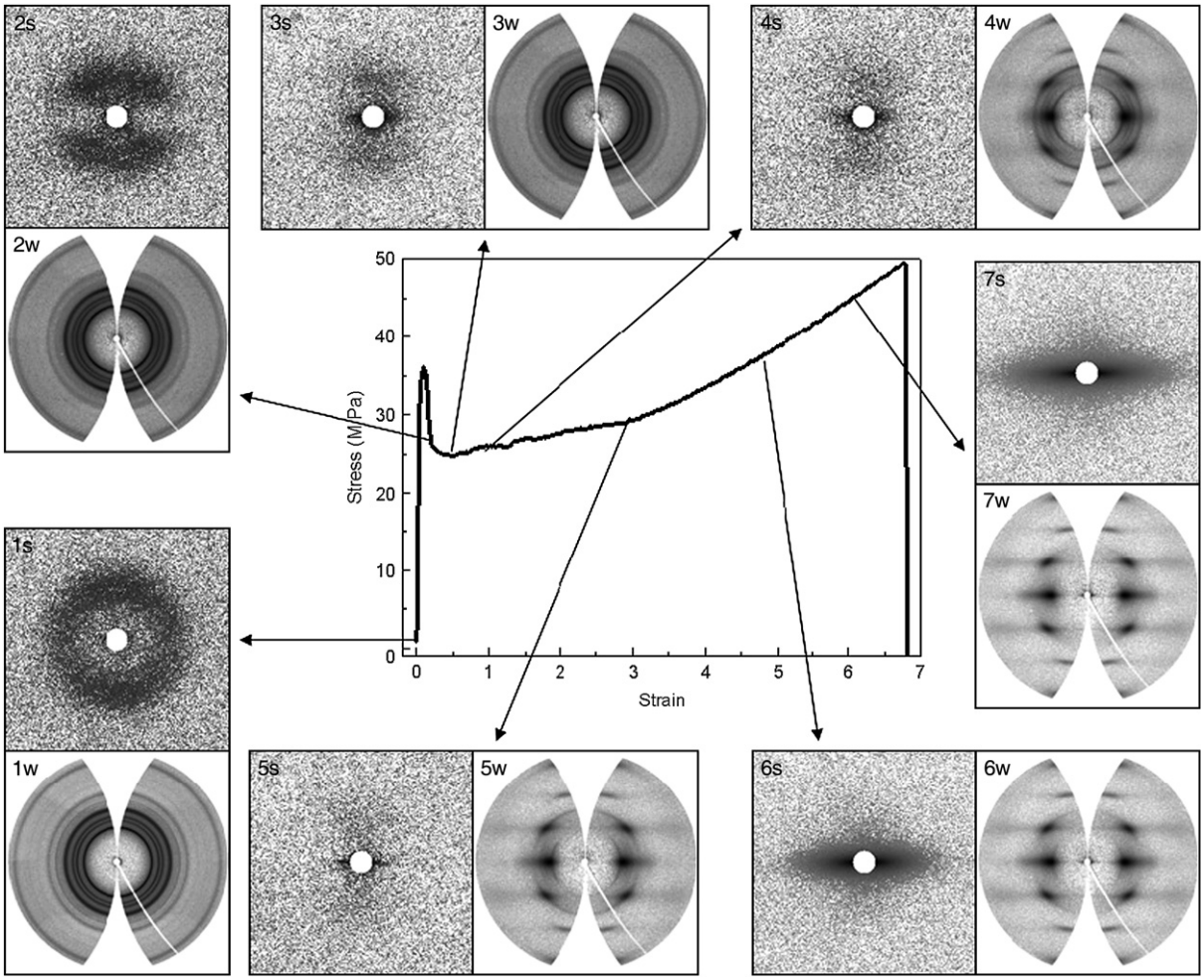

Fig. 2. Engineering stress–strain curve and selected 2D SAXS and WAXD patterns acquired during uniaxial tensile deformation of iPP films at room temperature.

between the adjacent lamellae, was estimated from the position of scattering peak using Bragg's law. The estimated long period in the iPP sample at room temperature before deformation was about 11 nm.

A yield point was seen soon after deformation began, at a strain of 0.1. The subsequent stress dropped rapidly and then increased with strain, where a two-staged linear stress–strain response was seen. The initial stage (at strains between 0.1 and 3.0) exhibited a small stress–strain ratio. The final stage (at strains between 3.0 and 7.0) exhibited a large stress–strain ratio, which could be attributed to the dominant process of strain-induced crystallization (sometimes termed the strain-hardening stage). It was found that the corresponding 2D WAXD patterns changed dramatically after the yield point. Not only did the azimuthal spreads of all isotropic diffraction rings become narrower, also the diffraction peak widths became broader, especially along the equator. The azimuthal spread of the (110) reflection peak and the linear diffraction intensity profile taken along the equator from WAXD at different strains is illustrated in Fig. 3A and B, respectively. In Fig. 3B, four distinct diffraction peaks: (110), (040), (130) and (111)/(041) (from left to right), were seen in the undeformed sample. The diffraction intensity from the (110) reflection was strong but it was nearly azimuthally independent, indicating the presence of a small degree of preferred orientation. Upon deformation, the intensities of these diffraction peaks decreased notably. In particular, at strain = 0.35, the (110) reflection on the meridian vanished rapidly, resulting in four peaks at the off-axis (Fig. 3A). Such a behavior, along with the observation of decreasing intensity in the (110) reflection (Fig. 3B), suggested that selective melting and rearranging of the residual structure took place. At strain = 0.58, a notable change in the structure was seen, as evidenced by the drastic increase of the equatorial (110) peak, while two off-axis shoulders remained visible (Fig. 3A). The appearance of the strong equatorial (110) peak was probably due to the combined contributions of highly reoriented "original" crystals, strain-induced "new" crystals and the mesomorphic phase. The presence of weak off-axis (110) shoulders was probably dominated by the diffraction of partially oriented "original" crystals. The corresponding linear WAXD profile along the equator showed one broad peak, covering the angular range of (110), (040) and (130). The other two diffraction peaks, (111) and (041), vanished on the equator but became stronger on off-axis. The peak broadening on the equator can be attributed to the formation of the oriented mesomorphic phase, which will be discussed later. At higher strains (>0.6 till break), the off-axis (110) peaks weakened significantly due to the further melting or/and reorientation of partially oriented "original" crystals, while the equatorial (110) peak increased and became broader due to the growth of the oriented mesomorphic phase. The corresponding 3D WAXD patterns are illustrated in Fig. 4. These patterns showed a clear structure change from crystal to mesomorphic phases.

The changes of mass fractions from different phases are illustrated in Fig. 5. It was seen that, at the initial stage of uniaxial tensile deformation (strain < 1.0), both fractions of crystal and amorphous phases decreased with strain, while the corresponding fraction of oriented mesomorphic phase increased rapidly. This suggests that, at room temperature, some crystals were destroyed, where the oriented mesomorphic phase was formed from both stretched amorphous phase and destroyed crystal phase. The possible mechanism of this transition will be discussed later. At strains above 1.0, the fraction of crystal phase began to increase at a rate similar to that of the oriented mesomorphic phase. The slight increase of the crystals fraction can be attributed to several coupled effects: (1) destruction of "original" crystals, (2) reorientation of "original" crystals (since the fraction of unoriented crystals continued to decrease) and (3) formation of highly oriented "new" crystals (may be in the form of extended-chain crystals). It is interesting to note that the fraction of oriented crystal phase exhibited a minimum value at the strain

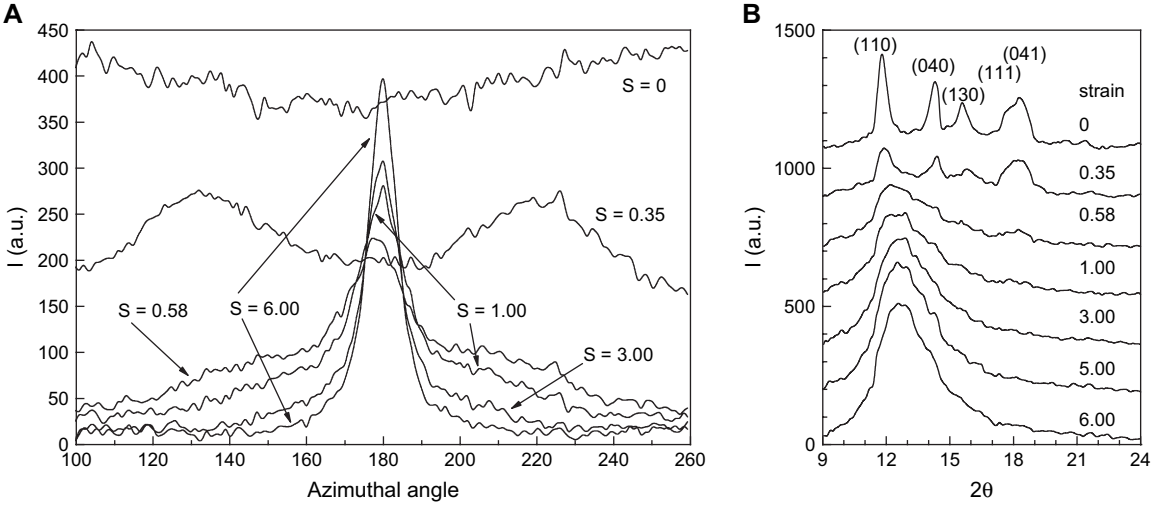

Fig. 3. (A) The azimuthal spread of the (110) peak at varying strains, and (B) linear diffraction intensity profiles taken along the equatorial direction at different strains.

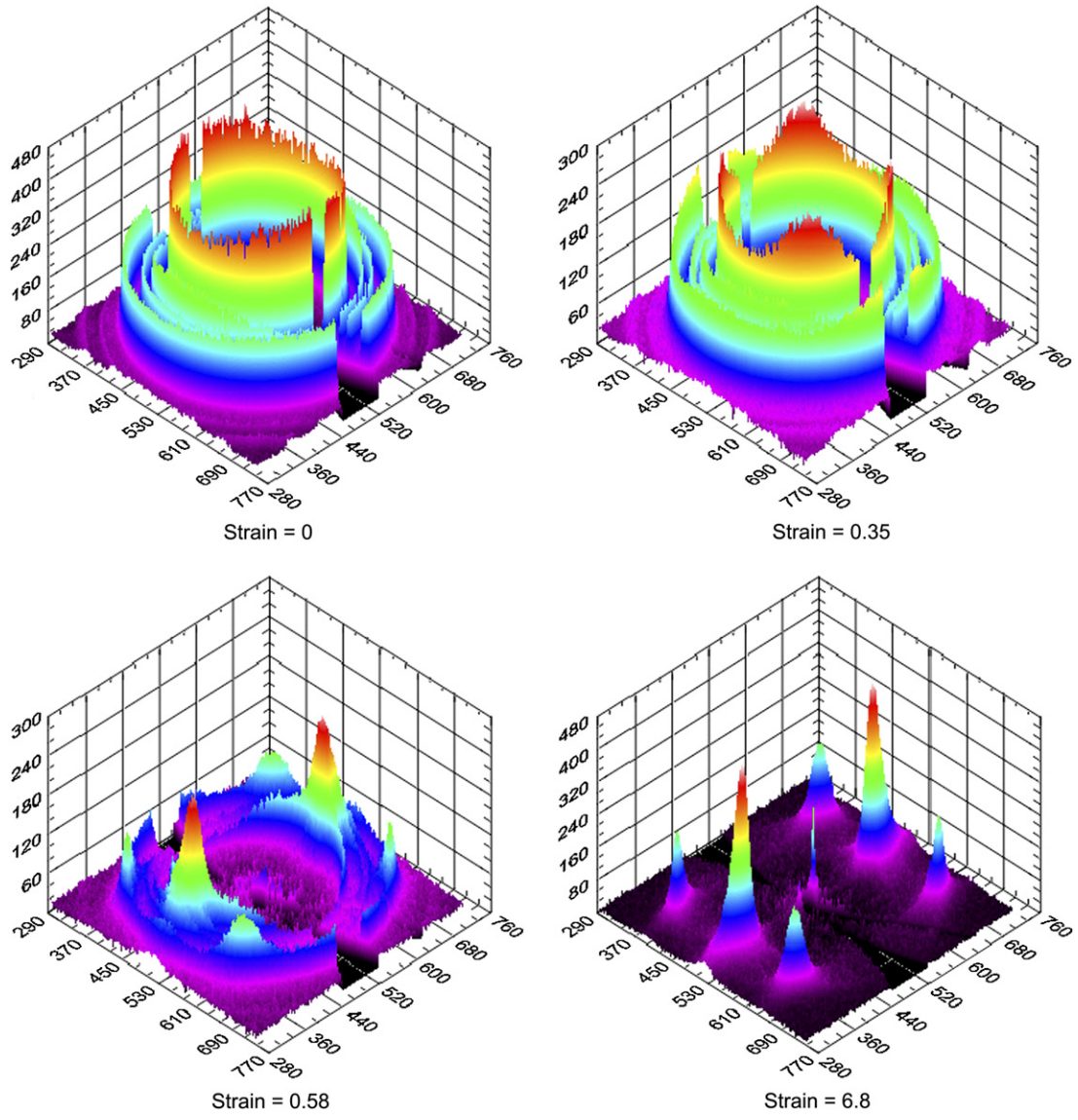

Fig. 4. 3D WAXD patterns during uniaxial tensile deformation at room temperature.

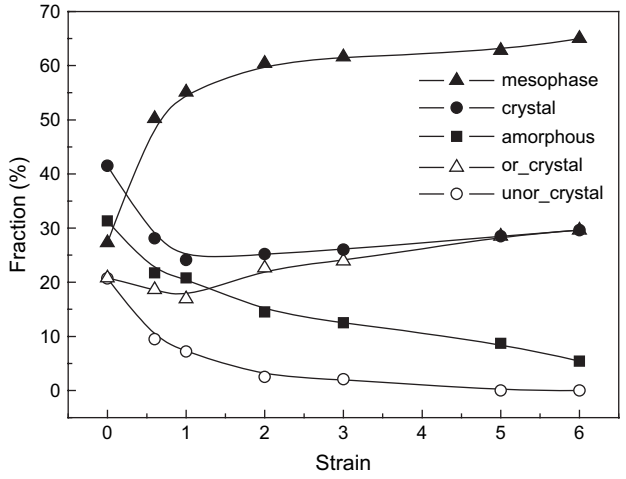

Fig. 5. Evolution of the fractions of amorphous, mesomorphic and crystal (including oriented crystal and unoriented crystal) phases in the iPP film during uniaxial tensile deformation at room temperature.

of about 1.0, whereas the fraction of unoriented crystal phase decreased monotonically. At high strains (i.e., >5.0), the unoriented crystals vanished completely, leaving behind only unoriented amorphous, oriented crystal and oriented mesomorphic phases (the fraction of mesomorphic phase was above 60%, the fraction of oriented crystal phase was about 30%, and the fraction of unoriented amorphous phase was less than 10%).

Selected 3D SAXS patterns during deformation are illustrated in Fig. 6. It was seen that upon stretching, the initial isotropic scattering ring in the SAXS pattern became two-bar like, which gradually disappeared with increasing strain. This is reasonable since the density of the crystal phase is slightly larger than that of the mesomorphic phase, the formation of oriented mesomorphic phase will gradually decrease the scattered intensity. The two-bar SAXS pattern on the meridian indicated two possible scenarios. (1) The "original" lamellar stacks that were parallel to the stretching direction

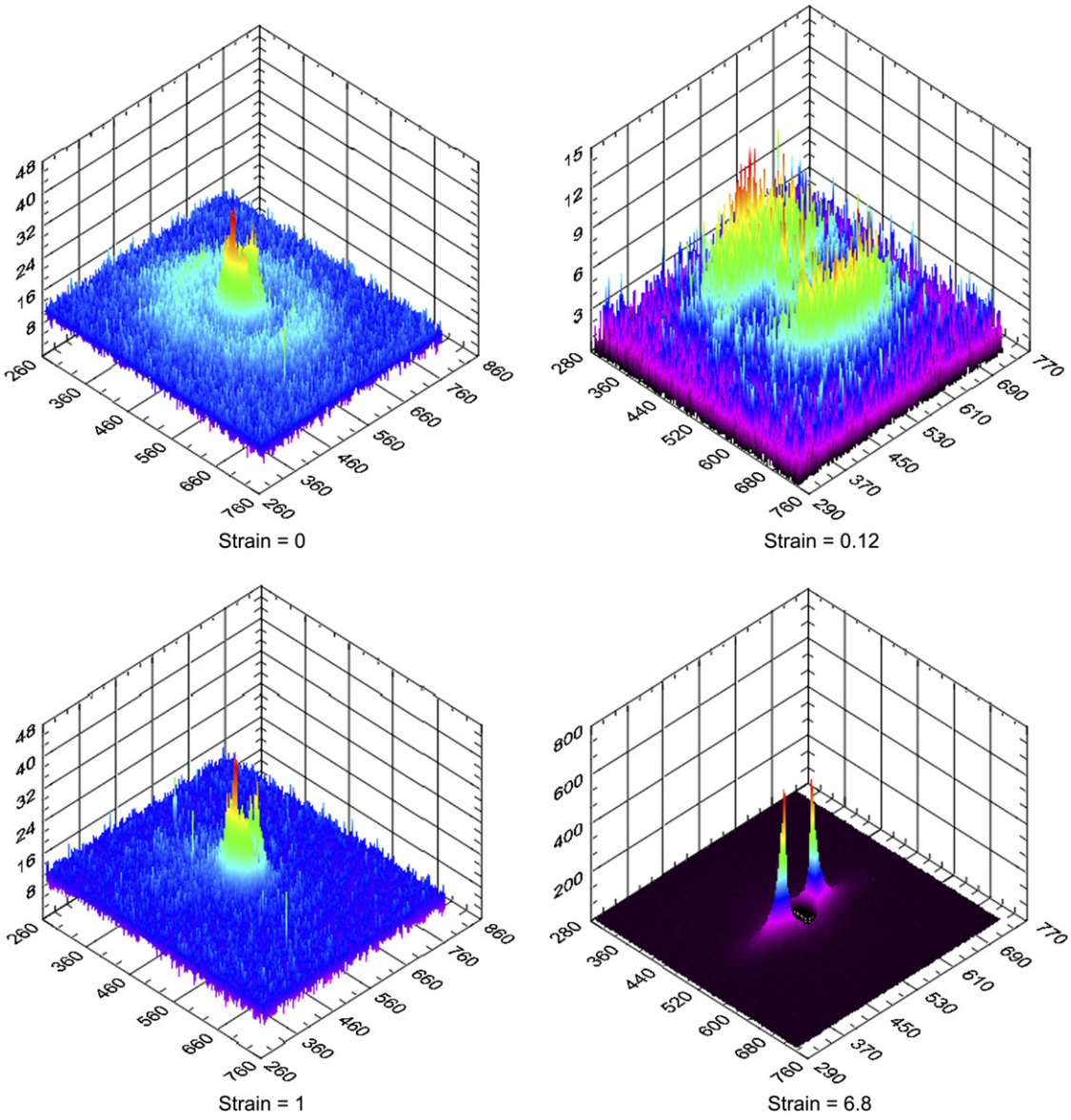

Fig. 6. 3D SAXS patterns during uniaxial tensile deformation at room temperature.

were destroyed (e.g. by chain pulling-out). (2) The ''original'' lamellar stacks became fragmented and reoriented along the direction perpendicular to the stretching direction. It was found that the long period increased from 11.1 nm to 11.8 nm and 12.8 nm at strains of 0.0, 0.1 and 0.4, respectively. Uniaxial tensile deformation clearly enlarged the average distance between the lamellae along the stretching direction. However, due to the small density difference between the mesomorphic and crystal phases at room temperature as well as the reduced thickness of the sample during deformation, the SAXS intensity became quite weak. At the later stage of deformation, the SAXS pattern exhibited a strong equatorial streak, probably due to stress-induced micro-voids (the dominant contribution) and strain-induced crystalline fibrils (the minor contribution) arising during deformation until the stretched iPP film was broken at a strain of about 6.8.

3.2. Uniaxial tensile deformation at high temperatures (60 °C and 160 °C)

Uniaxial tensile deformation of iPP film was also carried out at two higher temperatures: 60 and 160 °C. The engineering stress–strain curve and selected 2D WAXD and SAXS patterns obtained at 60 °C are illustrated in Fig. 7. The observed engineering stress–strain curve was generally similar to that obtained at room temperature. However, distinct structure differences were also seen. The linear WAXD profiles along the equatorial direction extracted from Fig. 7 are illustrated in Fig. 8. It was found that the orientation of iPP crystal structure occurred at a much higher strain than that at room temperature, evidenced by the disappearance of the (111)/(041) doublet peak on the equator. At room temperature, this doublet migrated to off-axis position at a strain of about 1.0, while this shift took place at a strain of about 2.0 at 60 °C. It was interesting to

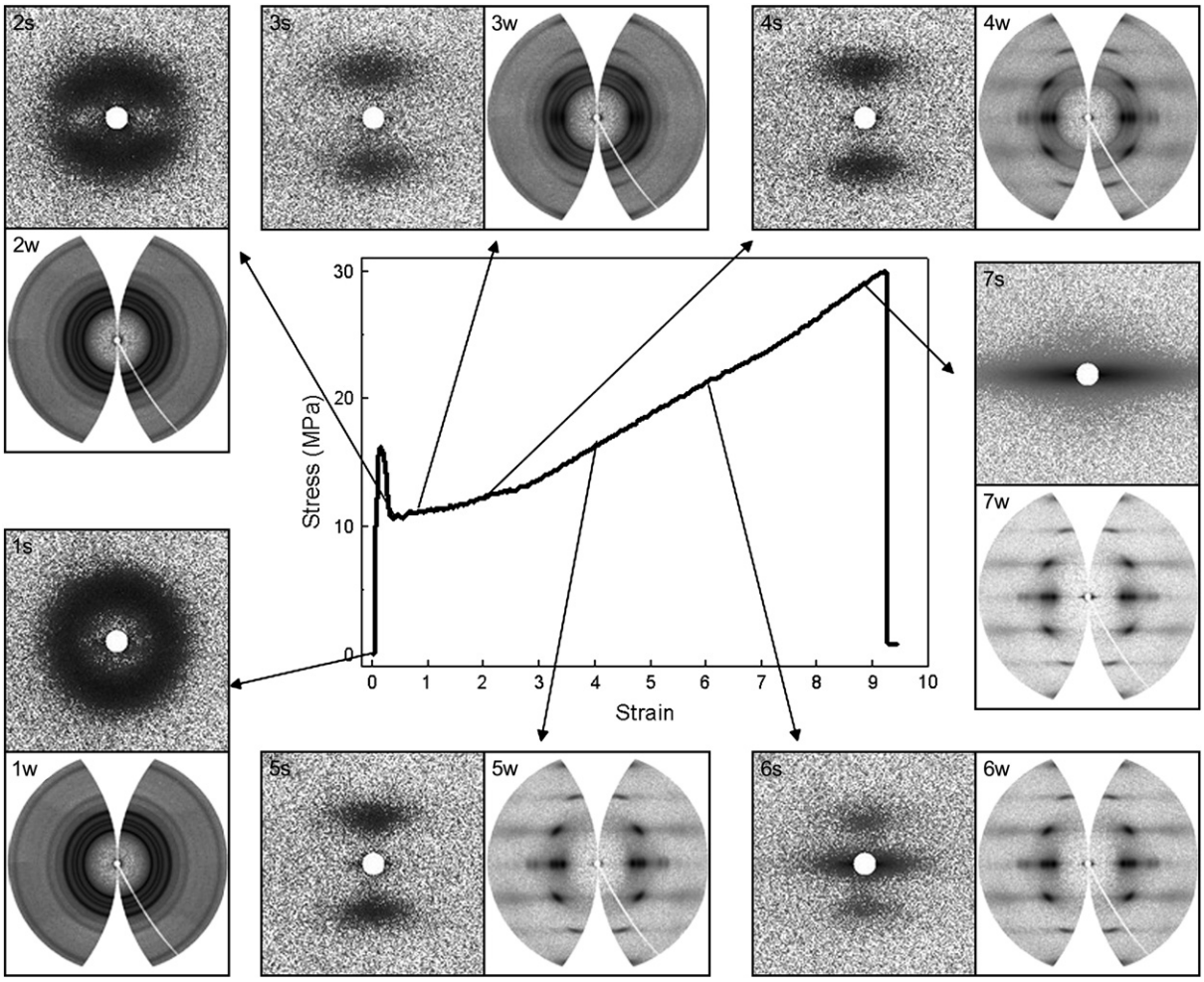

Fig. 7. Engineering stress–strain curve and selected 2D SAXS and WAXD patterns acquired during uniaxial tensile deformation of iPP films at 60 °C.

note that the α-form crystal structure never vanished during deformation, where three distinct diffraction peaks ((110), (040) and (130)) could be seen even at a high strain of 9.0 before breaking. However, these three peaks overlapped with each other to some extent, indicating that both crystal and mesomorphic phases co-existed at high strains.

The mass fractions of different phases (amorphous, mesomorphic and crystal, including oriented and unoriented crystals) during deformation are illustrated in Fig. 9. Similar to the case at room temperature, the fraction of oriented mesomorphic phase increased with strain. However, the fraction of the total crystal phase increased slightly at strains >1.0, instead of decreasing as seen at room temperature. The total crystallinity increase was mainly due to the increase in oriented crystals, since the fraction of unoriented crystals decreased upon deformation. This suggests that the crystal destruction is a minor event. The major events were the orientation of some ''originated'' crystals and formation of ''new'' crystals. The notable increase of the oriented mesomorphic phase could be mainly attributed to the decrease in the amorphous phase fraction.

Uniaxial tensile deformation was also carried out at 160 °C, near the melting point of iPP, and the results are shown in Fig. 10. Under this condition, the elongation-to-break ratio (at a strain >16.0, which was the limit of our heating chamber) was significantly larger than those at lower temperatures. From corresponding 2D WAXD and SAXS patterns, the azimuthal spreads for both diffraction and scattering peaks became quite narrow with increasing strain, indicating the increase in orientation at both crystal structure and lamellar scales. The linear WAXD profiles taken along the equatorial direction are illustrated in Fig. 11. Different from the cases under room temperature and 60 °C, no peak broadening was found during deformation at 160 °C. It was seen that the intensities of all equatorial peaks increased drastically with strain, and the apparent crystallinity remained high even near the melting point. At strains higher than 10.0, the (111) and (041) doublet peaks disappeared from the equator (they moved to the off-axis); but (150) and (060), corresponding to 2θ of 21.9°, and (200) reflection, corresponding to 2θ of 24.2°, remained visible. The full widths at half maximum (FWHM) of reflections from (110), (040) and (130) crystal planes all showed a two-staged increase with strain (a rapid increase at low stains and a slow increase at high strains) at all temperatures during deformation. The value of FWHM is related to the combined effects of crystal size and lattice distortion.

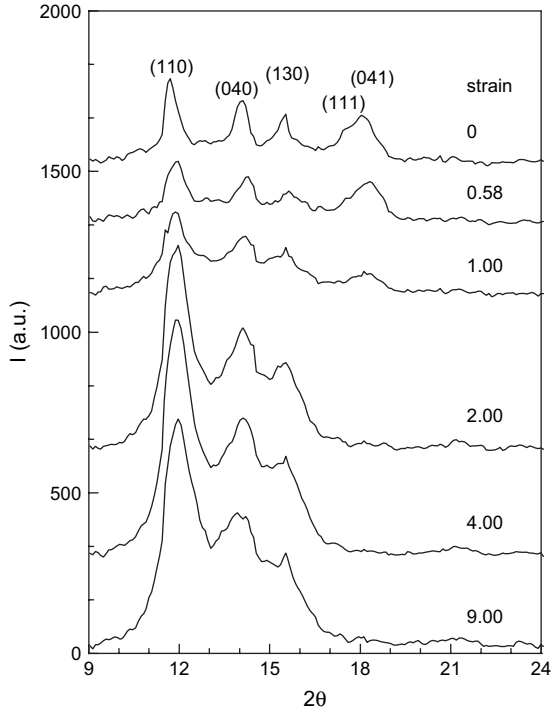

Fig. 8. Linear WAXD profiles along the equatorial direction at different strains during uniaxial tensile deformation.

From the 2D SAXS patterns in Fig. 10, the following observations were made. Above the "yield" point (at strain of about 1.0), the scattering maxima quickly converged onto the meridian, forming a two-bar pattern, indicating that the crystal fragmentation also occurred at 160 °C. However, by comparing with the SAXS patterns at 60 °C, the high temperature SAXS pattern showed a smaller scattering bar, indicating a larger lamellar structure. It appeared that less crystal fragmentation took place at 160 °C than that at low temperatures (room temperature and 60 °C). The total scattered intensity was found to increase with strain, probably due to the partial melting of small crystals or/and the decrease of the mesomorphic fraction, and both could enhance the scattering contrast. The average long period along the meridian during deformation at 160 °C was larger than those at lower temperatures. It was interesting to note that an equatorial streak appeared at strains above 2.0 and it increased with increasing strain. This streak feature, judging by its much weaker intensity (than those of room temperature and 60 °C), was probably resulted mainly from the fibrillar morphology instead of micro-voids. This is because the scattered intensity from micro-voids should be significantly higher due to the larger density contrast (we note that the streak intensity at 160 °C was only about several percent of those at room temperature and 60 °C).

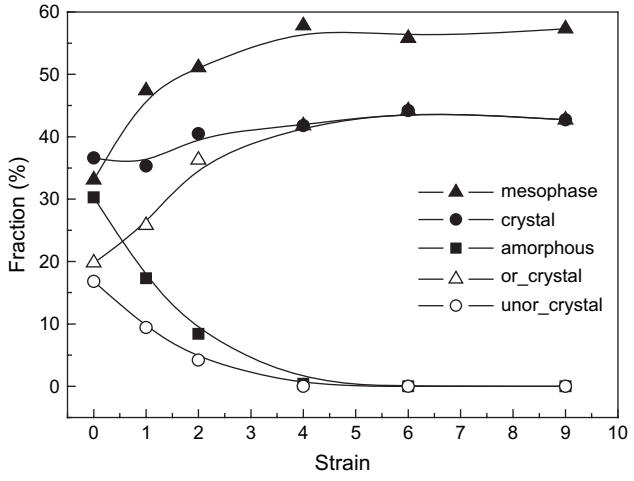

Fig. 9. Evolution of mass fractions of amorphous, mesomorphic and crystal (including oriented crystal and unoriented crystal) phases in the iPP film during uniaxial tensile deformation at 60 °C.

The linear intensity profiles taken along the meridional direction of the 2D SAXS patterns are illustrated in Fig. 12(A). It is interesting to note that at the initial stage of deformation, the position of the scattering peak shifted to a lower q value; upon further deformation, it shifted back to near the original position [52]. The corresponding long period for the lamellae structure estimated by Bragg's law is plotted in Fig. 12(B). The increase in long period at strains <1.0 could be attributed to the elastic deformation of iPP crystals. The long period was found to decrease at strains between 1.0 and 3.0 (the maximum long period value was seen at strain = 1.0), and then it reached a plateau value of 32 nm at strains between 3.0 and 11.0. This behavior can be explained by the fragmentation and the strain-induced crystallization coupled with slippage process between fragmented crystal and strain-induced melting. Based on the WAXD results, we argue that the formed strain-induced crystals at 160 °C are in the form of lamellae with folded-chain conformation. The long period was found to decrease again at strains >11.0, which might be due to the limitation of slippage.

The evolution of mass fractions for different phases during deformation at 160 °C is shown in Fig. 13. It is seen that the fraction of amorphous phase decreased continuously and nearly disappeared at strain = 16.0, but we do observe a clear SAXS pattern at the end of deformation indicating the electron density difference between amorphous and crystal phase. The reason is probably due to the limitation of our analysis method, since the amorphous phase can also be oriented slightly resulting in more scattering intensity at the equator which is attributed to the mesophase during analysis. The total crystal fraction showed a two-staged increase with a faster rate at low strains (<2.0) and a slower rate at high strains (>2.0). The change of oriented crystal fraction was similar to that of total crystal fraction, but with an enhanced magnitude at the initial stage. The difference was due to the variation of unoriented crystal fraction, which showed a maximum value at strain = 1.0. This response was consistent with the observed maximum long period also at strain = 1.0. In contrast to the large increase at lower temperatures (room temperature and 60 °C), the fraction of mesomorphic phase was constant (at about 35%) during deformation at 160 °C. This suggests that the major transition induced by deformation at this temperature is mainly between the amorphous and crystal phases. The above findings are consistent with the hypothesis that

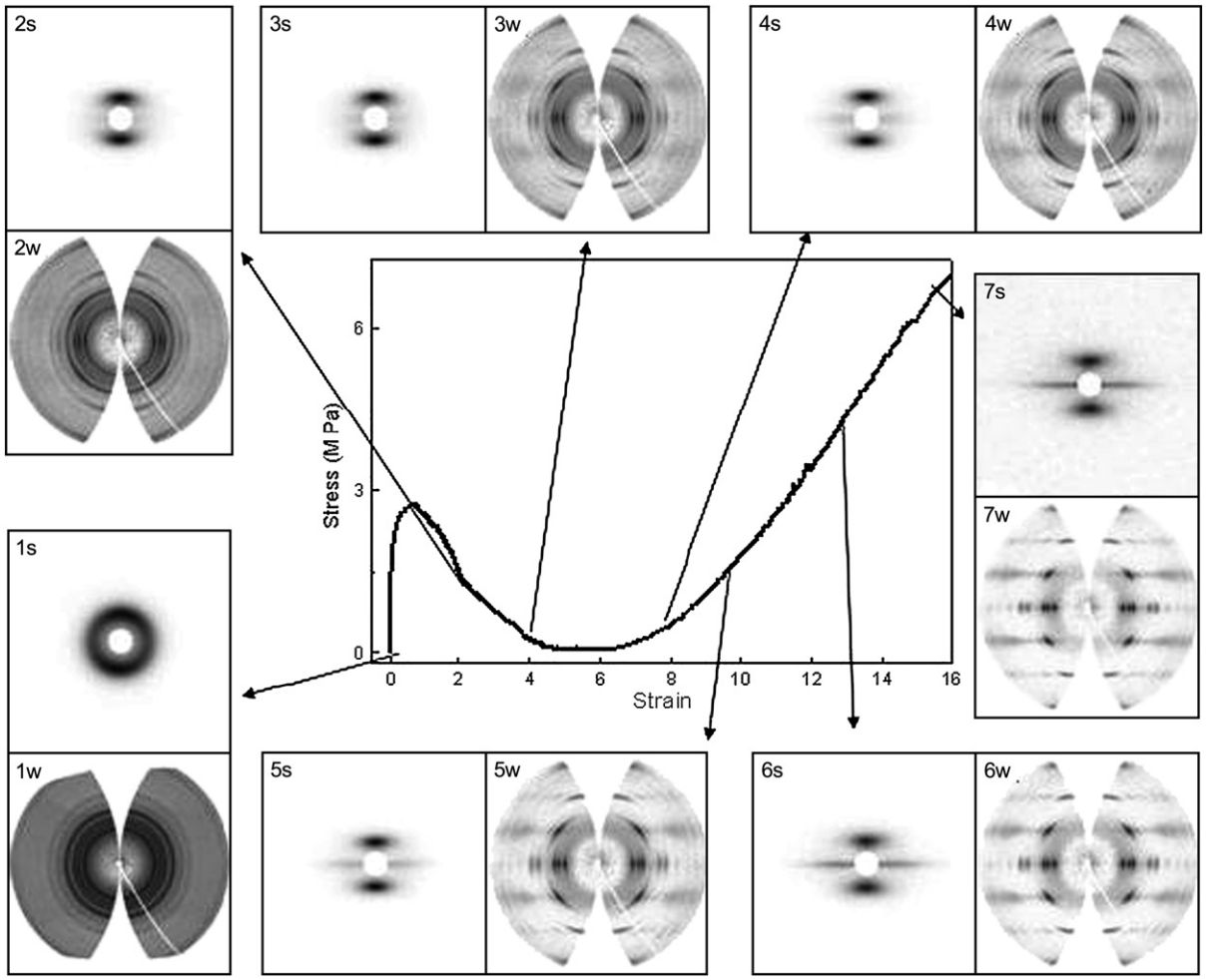

Fig. 10. Engineering stress–strain curve and selected 2D SAXS and WAXD patterns acquired during stretching of iPP films at 160 °C.

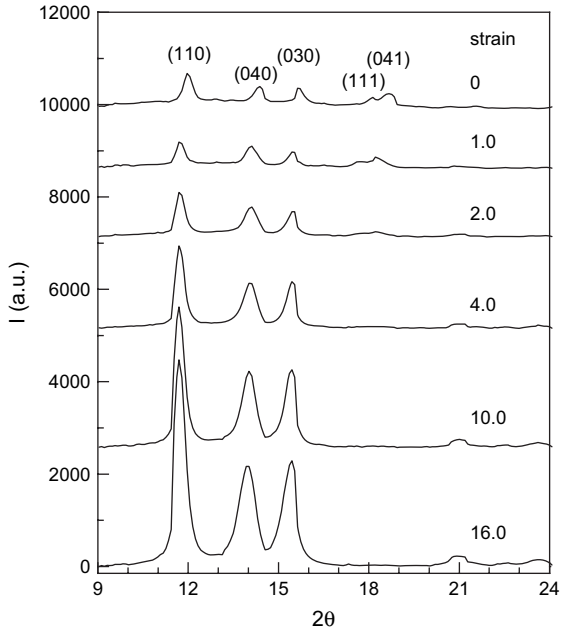

Fig. 11. Linear WAXD profiles along the equatorial direction at different strains during stretching of iPP film at 160 °C.

entangled coiled chains are crystallized into lamellar crystals with folded-chain conformation [69] under low strains near the nominal melting point (160 °C), and can be disentangled at very high strains (e.g. at strain = 16.0).

3.3. Morphology and crystal orientation during deformation at varying temperatures

In order to develop a reasonable molecular mechanism to explain the above observations, we have also compared the AFM results with combined SAXS and WAXD images of three representative morphologies from quenched samples prepared under different deformation conditions. The comparisons are shown in Fig. 14. In the undeformed initial iPP sample, a distinct spherulitic morphology with very slight orientation was seen (probably caused by an uneven squeeze flow during melt pressing). This was consistent with WAXD and SAXS images, which also showed slightly oriented diffraction and scattering rings. When the iPP film was stretched to a strain of 4.0 at 60 °C, the AFM image exhibited a distinct fibrillar structure with fibrils aligned parallel to each other along the stretching direction, consistent with the two meridional

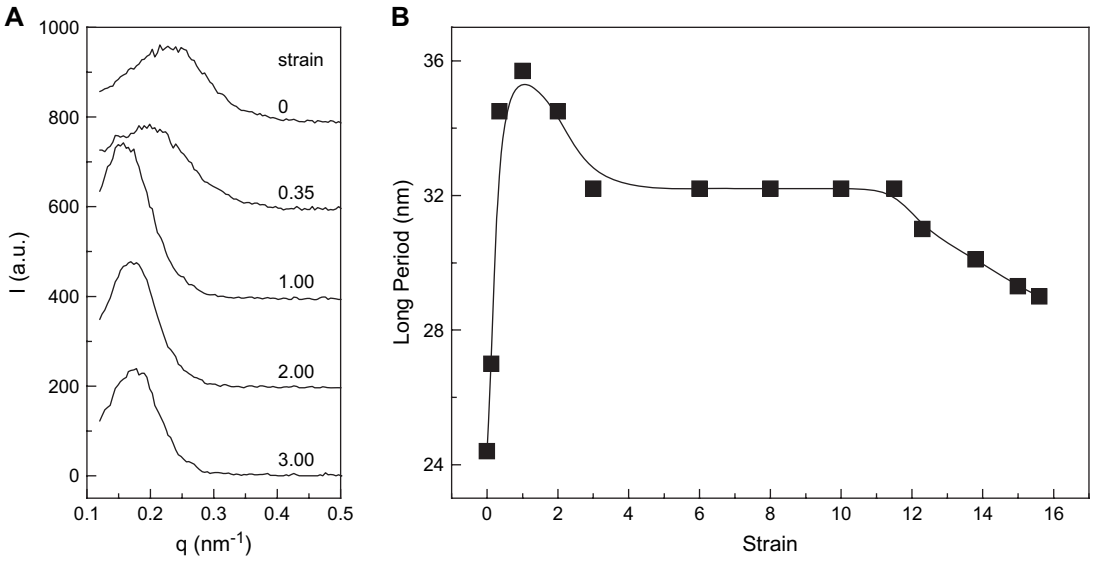

Fig. 12. (A) Linear SAXS intensity profiles taken along the meridional direction at different strains during uniaxial tensile deformation, and (B) corresponding change of long period as a function of strain.

scattering bars in the SAXS pattern arising due to the well-oriented and correlated layered-like folded-chain lamellae. The narrow azimuthal spreads of the WAXD peaks indicated that the crystal (α-form) orientation increased with the draw ratio. However, the analysis showed that the mass fraction of oriented mesomorphic phase was larger than 50% and that of oriented crystal phase was about 40%, indicating the co-existence of mixed lamellar crystals (in α-form) and mesomorphic (with no preferred registration of helical hands) structures. We note that it is not possible to distinguish the crystal and mesomorphic phases from AFM measurements. This is because there is not much difference in the modulus and hardness between the two phases, where the AFM technique cannot probe into the structures of the ordered domains. Nevertheless, the structure difference became very distinct by the X-ray diffraction technique. It was interesting to see that when the iPP film was stretched to the strain of 16.0 at 160 °C, a very weak equatorial streak was still remained, which could be attributed to the presence of extended-chain mesomorphic microfibrils instead of micro-voids since the latter could not be found by AFM measurements of the quenched iPP film. The existence of the two-bar pattern at a lower scattering angle indicated the persistence of a highly oriented crystal lamellar structure with a larger spacing. This was also consistent with the WAXD pattern exhibiting well-oriented α-form crystals.

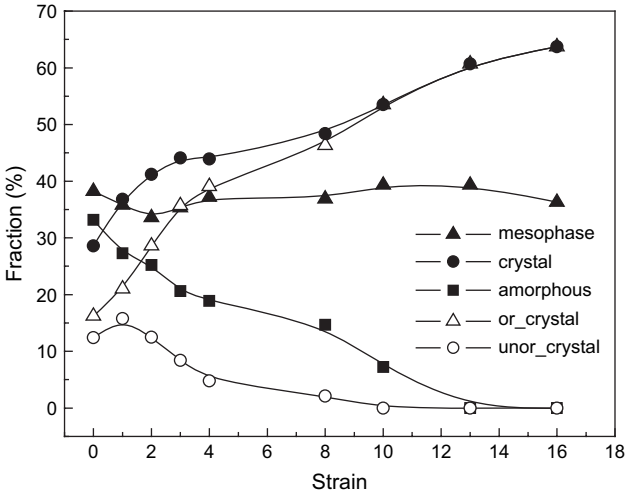

Fig. 13. Evolution of mass fractions of amorphous, mesomorphic and crystal (including oriented crystal and unoriented crystal) phases in the iPP film during uniaxial tensile deformation at 160 °C.

The chain orientation (f) in the crystal structure can be calculated by Hermans' orientation function [70]:

$$f = \frac{3\langle\cos^2\phi\rangle - 1}{2}$$

where ϕ is the angle between the chain axis and the reference axis (stretching direction); $\langle\cos^2\phi\rangle$ is defined as:

$$\langle\cos^2\phi\rangle = \frac{\int_0^{\pi/2} I(\phi)\cos^2\phi\sin\phi\,\mathrm{d}\phi}{\int_0^{\pi/2} I(\phi)\sin\phi\,\mathrm{d}\phi}$$

where $I(\phi)$ is the scattered intensity along the angle ϕ. However, since there is no plane of symmetry perpendicular to the chain axis, $\langle\cos^2\phi\rangle$ is calculated from the crystal (110) and (040) reflections.

$$\langle\cos^2\phi\rangle = 1 - 1.090\langle\cos^2\phi_{110}\rangle - 0.901\langle\cos^2\phi_{040}\rangle$$

The calculated Hermans' orientation factors are shown in Fig. 15. It was seen that the initial sample possessed a value

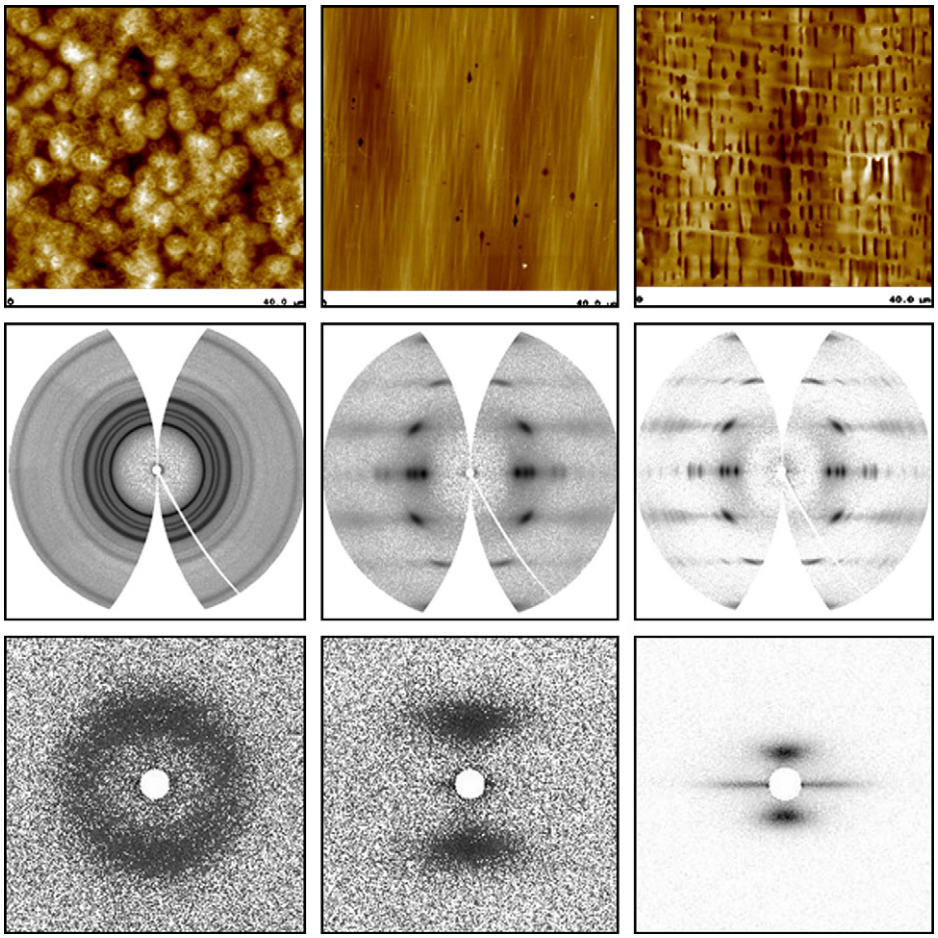

Fig. 14. AFM, WAXD and SAXS images of iPP film under different conditions. Left column: spherulitical morphology (strain = 0.0, T = RT); center column: fibrillar structure (strain = 4.0, T = 60 °C); right column: voids and transverse bands (strain = 16.0, T = 160 °C). (AFM scale: 40 μm.)

of about zero, representing a random orientation of polymer crystals (in the lamellar form). During stretching, the crystal alignment increased asymptotically toward the value of one, representing the perfect alignment of polymer chains in lamellar crystals along the stretching direction. The rate of crystal alignment during deformation at high temperatures was found to be slower than that at low temperature, but the final orientation during deformation at high temperatures was higher due to the higher applied strain.

3.4. The role of interlamellar chain entanglement in deformation-induced structure changes

The mechanical properties of semi-crystalline polymers have been considered from the viewpoint of crystallinity, crystalline morphology and tie chains. Tie chains are often thought of as tightly stretched chain segments connecting the adjacent crystal lamellae. Higher tie chain concentration can lead to stronger mechanical properties. This conventional concept of tie chains is clearly related to the subject of this study, but it can only be used to explain parts of the experimental results. This is because the presence of tie chains will initiate the fragmentation of folded-chain lamellae at high strains, which is consistent with the results from deformation at lower temperatures, but it should not increase the fraction of folded-chain lamellar crystals at high strains as observed at high temperatures.

Based on experimental observations in this study, we present a new mechanism that can explain deformation results at both low and high temperatures. The mechanism considers

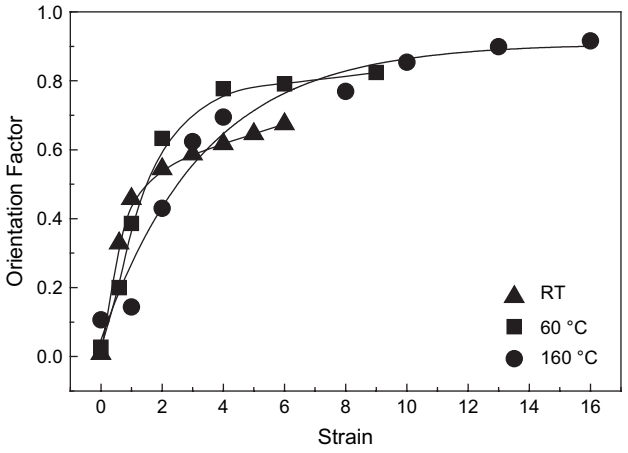

Fig. 15. Hermans' orientation factors of crystal chain axis as a function of strain for iPP film at different temperatures.

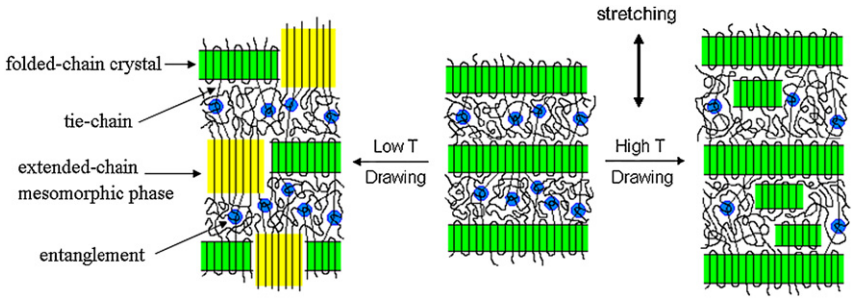

Fig. 16. The deformation of the crystal and amorphous phases during uniaxial tensile deformation at low and high temperatures.

the role of chain entanglement in the interlamellar amorphous layers. As described earlier, if the total entanglement density in the sample is not decreased by folded-chain crystallization, the resulting entanglement density in the interlamellar amorphous region after crystallization will be higher than that in the initial bulk melt. We hypothesize that tie chains are mainly due to the consequence of chain entanglements, which carry the major mechanical load in the interlamellar amorphous region. Of course, some tie chains can also occur without the presence of chain entanglement, but the fraction may be small. In the above mechanism, two scenarios may occur. (1) The distribution of tie chains may be heterogeneous in the interlamellar region as they will be concentrated mostly around the vicinity of the entanglement. (2) Some amorphous chains or chain segments without the influence of chain entanglement may not carry any mechanical load during mechanical deformation. The second scenario is consistent with the persistent observation of amorphous fraction at low strains under both low and high temperatures.

The role of chain entanglement and its relationship with tie chains during deformation-induced structure change in semicrystalline polymers is schematically illustrated in Fig. 16. In the middle diagram, a typical folded-chain lamellar assembly (colored in green) is shown, where the frozen entanglement points (colored in blue) are confined in the interlamellar amorphous region (for interpretation of the references to color in this figure, the reader is referred to the web version of this article). During stretching at low temperatures (e.g. room temperature), the poor chain mobility would restrict the motion of chain slipping and thus chain disentanglement. As a result, the local stress concentration of the entanglement will be strong, resulting in the fragmentation of neighboring crystal lamella by chain pull-out (often referred as mechanical melting). In iPP, the stretched-out chains can transform into the oriented mesomorphic phase (colored in yellow, left diagram of Fig. 16) having extended-chain conformation but without the regular registration of helical hands as in the crystal form. At high temperatures (e.g. at 160 °C), the enhanced chain mobility can significantly weaken the amorphous entanglement network. As a result, the tensile deformation would lead to chain disentanglement, reducing the constraints for folded-chain crystallization from interlamellar coiled segments. This would be consistent with the increase in folded-chain crystals during deformation at high temperatures, as shown in Figs. 13 and 16. We noted that the fraction of the mesomorphic phase remained constant during deformation at 160 °C, suggesting that the pre-existing structure of the mesomorphic phase might not be significantly affected by deformation (except that it became much more oriented). In the case of deformation at an intermediate temperature (e.g. 60 °C), the scenario may be in between the two cases described above, depending on the relative strength difference between the entanglement-induced tie chains and the adjacent crystalline lamellae. We note that the structure change during deformation at 60 °C is more similar to that at room temperature rather than that at 160 °C.

4. Conclusions

From the deformation study of iPP at three different temperatures (room temperature, 60 and 160 °C), we conclude that the role of chain entanglement in the interlamellar amorphous region plays an important role in affecting the structure. At low temperatures, as the chain mobility is relatively low (although the chain is still above the glass temperature), tie chains from entanglements may initiate the fragmentation of lamellar crystals upon stretching, forming oriented mesomorphic iPP phase with extended-chain conformation. This is consistent with both WAXD and SAXS results from deformation of iPP at room temperature and 60 °C. At high temperatures, as the chain mobility is relatively high, tensile deformation can lead to chain disentanglement allowing the formation of more folded-chain crystals from coiled segments. As a result, the fraction of the folded-chain crystal increases with strain, which is consistent with the results at 160 °C. The presence of tie chains is difficult to predict through conventional viewpoint, but the concept of chain entanglement-induced tie chains may permit us to correlate the melt rheology with the solid state chain topology in the amorphous domain and thus the final properties.

Acknowledgement

The authors acknowledge the financial support from the National Science Foundation (DMR-0405432) and the Dow Chemical Company. The assistance of Dr. Igors Sics and Dr. Lixia Rong for synchrotron SAXS and WAXD experimental setup is also greatly appreciated.

References

[1] Doi M, Edwards SF. The theory of polymer dynamics. Oxford: Clarendon Press; 1986.
[2] De Gennes PG. Scaling concepts in polymer physics. Ithaca: Cornell University Press; 1979.
[3] Rastogi S, Lippits DR, Peters GWM, Graf R, Yao Y, Spiess HW. Nat Mater 2005;4:635–41.
[4] Yamada K, Kamezawa M, Takayanagi M. J Appl Polym Sci 1981; 26:49–60.
[5] De Rosa C, Auriemma F, De Lucia G, Resconi L. Polymer 2005; 46:9461–75.
[6] Hong K, Rastogi A, Strobl G. Macromolecules 2004;37:10174–9.
[7] Al-Hussein M, Strobl G. Macromolecules 2002;35:8515–20.
[8] Schrauwen BAG, Janssen RPM, Govaert LE, Meijer HEH. Macromolecules 2004;37:6069–78.
[9] Schrauwen BAG, Breemen LCA, Spoelstra AB, Govaert LE, Peters GWM, Meijer HEH. Macromolecules 2004;37:8618–33.
[10] Keith HD, Padden FJJ, Vadimsky RG. J Polym Sci Part A-2 Polym Phys 1966;4:267–81.
[11] Lustiger A, Markham RL. Polymer 1983;24:1647–54.
[12] Huang Y, Brown N. J Polym Sci Part B Polym Phys 1991;29:129–37.
[13] Porter RS, Wang L. J Macromol Sci Rev in Macromol Chem Phys 1995;C35:63.
[14] Ishikawa M, Ushui K, Kondo Y, Hatada K, Gima S. Polymer 1996; 37:5375–9.
[15] Nitta K, Takayanagi M. J Polym Sci Part B Polym Phys 1999;37: 357–68.
[16] Janimak JJ, Stevens GC. J Mater Sci 2001;36:1879–84.
[17] Spitalsky Z, Bleha T. Polymer 2003;44:1603–11.
[18] Seguela R. J Polym Sci Part B Polym Phys 2005;43:1729–48.
[19] Hay IL, Keller A, Kolloid ZZ. Polymer 1965;204:43–74.
[20] Shimamura K. In Morphology of polymers: proceedings of 17th europhysics conference on macromolecular physics, Pargue, Czechoslovakia; 1985.
[21] Peterlin A. J Mater Sci 1971;6:490–508.
[22] Peterlin A. Colloid Polym Sci 1987;265:357–82.
[23] Flory P, Yoon D. Nature (London) 1978;272:226–9.
[24] Bowden P, Young R. J Mater Sci 1974;9:2034–51.
[25] Popli R, Mandelkern L. J Polym Sci Part B Polym Phys 1987;25: 441–83.
[26] Galeski A. Prog Polym Sci 2003;28:1643–99.
[27] Hiss R, Hobeika S, Lynn C, Strobl G. Macromolecules 1999;32: 4390–403.
[28] Ferreiro V, Coulon G. J Polym Sci Part B Polym Phys 2004;42:687–701.
[29] Hu WG, Schmidt-Rohr K. Acta Polym 1999;50:271–85.
[30] De Rosa C, Auriemma F, De Ballesteros OR. Phys Rev Lett 2006;96. 167801/1–4.
[31] Men Y, Riger J, Homeyer J. Macromolecules 2004;37:9481–8.
[32] Men Y, Rieger J, Strobl G. Phys Rev Lett 2003;91. 095502/1–4.
[33] Ran S, Zong X, Fang D, Hsiao BS, Chu B, Phillips RA. Macromolecules 2001;34:2569–78.
[34] Ran S, Zong X, Fang D, Hsiao BS, Chu B, Cunniff PM, et al. J Mater Sci 2001;36:3071–7.
[35] Ran S, Wang Z, Burger C, Chu B, Hsiao BS. Macromolecules 2002;35: 10102–7.
[36] Kawakami D, Ran S, Burger C, Fu B, Sics I, Hsiao BS. Macromolecules 2003;36:9275–80.
[37] Kawakami D, Ran S, Burger C, Fu B, Sics I, Hsiao BS, et al. Polymer 2004;45:905–18.
[38] Kawakami D, Hsiao BS, Ran S, Burger C, Avila-Orta C, Sics I, et al. Macromolecules 2005;38:91–103.
[39] Natta G, Peraldo M, Corradini P. Rend Accad Naz Lincei 1959;26:14.
[40] Natta G, Corradini P. Nuovo Cimento Suppl 1960;15:40.
[41] Wyckoff HW. J Polym Sci 1962;62(173):83–114.
[42] Morosoff N, Peterlin A. J Polym Sci Part A-2 Polym Phys 1972;10: 1237–54.
[43] Jones AT, Aizlewood JM, Beckett DR. Makromol Chem 1964;75:134.
[44] Brucker S, Meille SV, Petraccone V, Pirozzi B. Prog Polym Sci 1991; 16:361–404.
[45] Lotz B, Wittmann JC, Lovinger AJ. Polymer 1996;37:4979–92.
[46] Miller RL. Polymer 1960;1:135–43.
[47] Zannetti R, Celotti G, Fichera A, Francesconi R. Makromol Chem 1969;128:137.
[48] Zannetti R, Celotti G, Armigliato A. Eur Polym J 1970;6:879–89.
[49] De Candia F, Iannelli P, Staulo G, Vittoria V. Colloid Polym Sci 1988;266:608–13.
[50] Vittoria V. J Macromol Sci Phys Part B Phys 1989;B28(3 and 4):489–502.
[51] Song Y, Nitta K, Nemoto N. Macromolecules 2003;36:1955–61.
[52] Nozue Y, Shinohara Y, Ogawa Y, Sakurai T, Hori H, Kasahara T, et al. Macromolecules 2007;40:2036–45.
[53] Sakurai T, Nozue Y, Kasahara T, Mizunuma K, Yamaguchi N, Tashiro K, et al. Polymer 2005;46:8846–58.
[54] Koike Y, Cakmak M. Macromolecules 2004;37:2171–81.
[55] Koike Y, Cakmak M. Polymer 2003;44:4249–60.
[56] Koike Y, Cakmak M. J Polym Sci Part B Polym Phys 2006;44:925–41.
[57] Li JX, Cheung WL, Chan CM. Polymer 1999;40:3641–56.
[58] Li JX, Cheung WL, Chan CM. Polymer 1999;40:2089–102.
[59] Aboulfaraj M, G'Sell C, Ulrich B, Dahoun A. Polymer 1995;36:731–42.
[60] Zhang XC, Butler MF, Cameron RE. Polymer 2000;41:3797–807.
[61] Chu F, Yamaoka T, Kimura Y. Polymer 1995;36:2523–30.
[62] Huy TA, Adhikari R, Lupke T, Henning S, Michler GH. J Polym Sci Part B Polym Phys 2004;42:4478–88.
[63] Hong K, Strobl G. Macromolecules 2006;39:268–73.
[64] Wu J. Polymer 2003;44:8033–40.
[65] Aerts J. J Appl Crystallogr 1991;24:709–11.
[66] Wu J, Schultz JM, Yeh F, Hsiao BS, Chu B. Macromolecules 2000;33: 1765–77.
[67] Fraser RDB, Macrae TP, Miller A, Rowlands RJ. J Appl Crystallogr 1976;9:81–94.
[68] Ran S, Zong X, Fang D, Hsiao BS, Chu B, Ross R. J Appl Crystallogr 2000;33:1031–6.
[69] Dukovski I, Muthukumar M. J Chem Phys 2003;118:6648–55.
[70] Wilchinsky WZ. J Appl Phys 1960;31:1969–72.